
A QUASI-NEWTON METHOD FOR PHYSICALLY-ADMISSIBLE SIMULATION OF POISEUILLE FLOW UNDER FRACTURE PROPAGATION.

A PREPRINT

Guotong Ren

Department of Petroleum Engineering
University of Tulsa
Tulsa, OK 740104
guotong-ren@utulsa.edu

Rami M. Younis

Department of Petroleum Engineering
University of Tulsa
Tulsa, OK 74104
rami-younis@utulsa.edu

November 2, 2021

ABSTRACT

Coupled hydro-mechanical processes are of great importance to numerous engineering systems, e.g., hydraulic fracturing, geothermal energy, and carbon sequestration. Fluid flow in fractures is modeled after a Poiseuille law that relates the conductivity to the aperture by a cubic relation. Newton's method is commonly employed to solve the resulting discrete, nonlinear algebraic systems. It is demonstrated, however, that Newton's method will likely converge to nonphysical numerical solutions, resulting in estimates with a negative fracture aperture. A Quasi-Newton approach is developed to ensure global convergence to the physical solution. A fixed-point stability analysis demonstrates that both physical and nonphysical solutions are stable for Newton's method, whereas only physical solutions are stable for the proposed Quasi-Newton method. Additionally, it is also demonstrated that the Quasi-Newton method offers a contraction mapping along the iteration path. Numerical examples of fluid-driven fracture propagation demonstrate that the proposed solution method results in robust and computationally efficient performance.

Keywords Quasi-Newton, Fracture propagation, Coupled hydro-mechanics, Extended finite element method, Finite volume method.

1 Introduction

In hydro-mechanical processes, the interplay between rock deformation and fluid pressure in fractures can dictate first-order effects in several engineering systems such as hydraulic fracturing [2, 14], geothermal utilization [3], and CO₂ sequestration [5, 18]. In the limits of linearity, and assuming a constant positive-definite permeability tensor in fracture, existence and uniqueness of solution to the governing continuity equations has been established [7, 6]. The physically-accepted limit of Poiseuille flow introduces a nonlinear relation for fracture conductivity as a cubic function of local aperture. While formal conditions for the existence and uniqueness of solutions are well-established, numerical and semi-analytical approximations are widely applied. Newton's method is commonly employed to solve resulting algebraic equations whether it be in the contexts of fully- or sequentially-coupled solution processes. Numerical convergence difficulties can arise, as is generally the case with black-box nonlinear solution processes. More notably however, it is observed that the Newton iteration can converge to nonphysical solutions (i.e. aperture is negative). This is a frequently occurring issue and numerical evidence is easily obtained. Consider for example, a simple two-dimensional model with a fracture located at the center of a domain, and where fluid is injected into the mid-point of the fracture. Initially, the scaled fluid pressure and displacement fields are zero. Two alternate aperture profiles along the fracture are presented in fig. 1b; while both solutions satisfy the same nonlinear convergence criteria for the same model, one profile is oscillatory and includes negative aperture, whereas the other does not. Negative fracture (aperture) conductivity violates the positive-definite tensor requirement of [7, 6], and permits flow from low fluid

pressure to high fluid pressure. This simple example may support the hypothesis that the hydro-mechanical formulation possesses multiple solutions and that the nonphysical one can be obtained by application of Newton’s method. We omit the specifics of the numerical approximation and physical parameters employed in this illustrative example; in a subsequent section, it is demonstrated that the nonphysical solution exists regardless of the discretization employed.

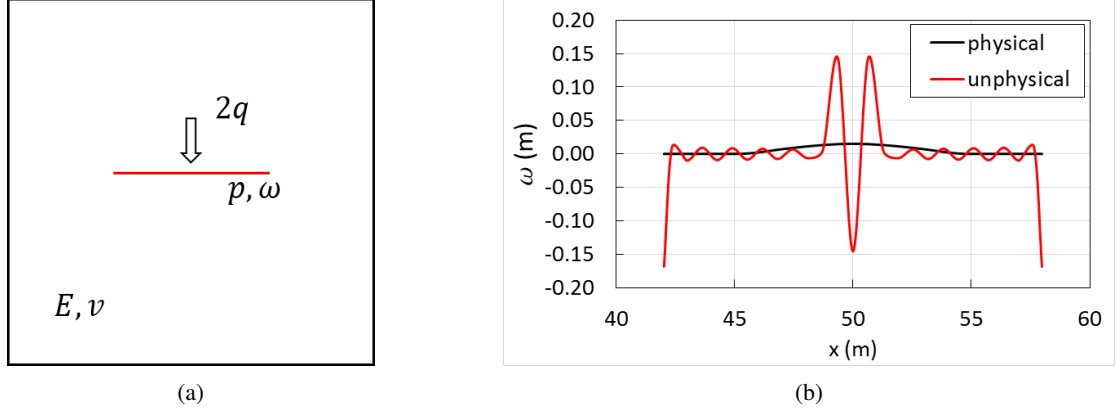


Figure 1: Example of multiple solutions: (a) case schematic; (b) aperture profile. The results are generated using coupled XFEM-FVM [15]

While significant to robust numerical simulation, the literature on the aforementioned issues is scarce. In this article, our focus is on linear elastic fracture propagation problems without fluid lag; i.e., fluid is assumed to occupy the entire fracture space at each instance in which the fracture tip reaches a failure state. Two classes of numerical fracture propagation simulation algorithm are: (1) Given a fixed tip advancement length step, determine the time increment such that tip is in an equilibrium failure state, and the solution satisfies the continuity equations (e.g., [9, 13, 15]); and (2) given a time step, determine the advancement length step for each tip such that the solution fulfills equilibrium failure (e.g., [8, 10]). In both classes of algorithm, the nonphysical solution may be encountered. [9, 15] propose initialization schemes for unknowns at every time that new fracture segments are introduced based on surrogate models. Nevertheless, while these initial guesses may improve convergence, it is observed that convergence to a nonphysical solution remains likely to occur in viscosity-dominated fracture propagation. [7] propose a safeguarding strategy by applying a relaxation to ω within the iterative coupled scheme. As $\omega < 0$ is detected during nonlinear iterations, the ω iterate is manually reassigned to a non-negative value. Although such an approach ensures a positive fracture conductivity should the method converge, an open question pertains to the effects on convergence rate and reliability.

A Quasi-Newton method is proposed to address global convergence to positive aperture solutions. The method proposes a Jacobian matrix modification that is inspired by that used in nonlinear two-point-flux finite volume methods (e.g. [12, 17]). For example in [12, 17], in order to maintain a monotone Jacobian matrix, derivatives of the transmissibility with respect to pressure are neglected. As a result, the converged pressure solutions are assured to be non-negative. For the fracture propagation problem and coupled hydro-mechanical problems at hand, monotonicity of the linearized operator is not guaranteed. For instance, the physical pressure solution may take on negative values near the tip region in the viscosity-dominated fracture propagation regime (fluid lag zones for example). Subsequently, the proposed approach will demonstrate that: (1) the fixed-point stability for the Newton’s and proposed Quasi-Newton methods are different; (2) the proposed Quasi-Newton method provides a contraction mapping property with Lipschitz constant between 0 and 1 on a designed iteration path; and (3) a non-negative aperture $\omega \geq 0$ is ensured at every nonlinear iteration.

Next, the mathematical formulation of the problem is detailed in section 2. Then, in section 3, the Quasi-Newton method is proposed and analyzed under the setting of an infinite domain where the mechanics equation can be formulated using a closed Green’s function between ω and pressure p . In section 3.2, the development is extended to more general fracture configurations. Specifically, we extend the algorithm to discretization using a coupled extended-finite-element method (XFEM) and finite volume method (FVM) for mechanics and flow, respectively [15].

2 Problem statement

Consider a spatial domain $\Omega \subset \mathbb{R}^2$ with external boundary Γ and its associated outward-oriented unit-normal \mathbf{n}_Γ . Dirichlet and Neumann boundaries for mechanics are Γ_u and Γ_t . The boundary segments are disjoint ($\Gamma_u \cap \Gamma_t = \emptyset$), and $\Gamma_u \cup \Gamma_t = \Gamma$.

A one-dimensional lower representation of the fracture, \mathcal{C} , is adopted. Fracture aperture, ω , is defined as,

$$\omega = \llbracket \mathbf{u} \rrbracket \cdot \mathbf{n}_c. \quad (1)$$

where $\llbracket \mathbf{u} \rrbracket$ is the jump of the displacement over the fracture, \mathbf{n}_c is the fracture unit-normal vector.

A single-phase incompressible fluid occupies fracture, and linear elastic mechanical deformation model is assumed. The continuity equation in the fracture is

$$\frac{\partial \omega}{\partial t} - \nabla_c \cdot \left(\frac{\omega^3}{12\mu} \nabla_c p \right) = 0 \quad \text{on } \mathcal{C}, \quad (2)$$

where ∇_c is the gradient operator defined on the fracture path. p is the fluid pressure in the fracture and μ is the fluid viscosity. Poiseuille's law posits that the fracture conductivity is $\frac{\omega^3}{12}$. The boundary condition at the inlet of the fracture is

$$-\frac{\omega^3}{12\mu} \frac{\partial p}{\partial x} = Q, \quad (3)$$

where Q is the fluid injection rate, and at the tip

$$-\frac{\omega^3}{12\mu} \frac{\partial p}{\partial x} = 0. \quad (4)$$

The quasi-static momentum equation reads

$$\nabla \cdot \boldsymbol{\sigma} = \mathbf{0}, \quad \text{on } \Omega, \quad (5)$$

where $\boldsymbol{\sigma}$ is the second order tensor. On the external boundary Γ , Neumann (force) and Dirichlet (displacement) conditions are

$$\boldsymbol{\sigma} \cdot \mathbf{n}_\Gamma = \mathbf{t} \quad \text{on } \Gamma_u, \quad (6a)$$

$$\mathbf{u} = \hat{\mathbf{u}} \quad \text{on } \Gamma_t, \quad (6b)$$

while on immersed fracture boundaries, p is imposed onto the oriented surfaces of the fracture:

$$\boldsymbol{\sigma} \cdot \mathbf{n}_c = p \mathbf{I} \cdot \mathbf{n}_c \quad \text{on } \mathcal{C}. \quad (7a)$$

The stress $\boldsymbol{\sigma}$ is modeled using linear elastic theory:

$$\boldsymbol{\sigma} = \frac{E\nu}{(1+\nu)(1-2\nu)} (\nabla \cdot \mathbf{u}) \mathbf{I} + \frac{E}{1+\nu} \boldsymbol{\varepsilon}, \quad (8)$$

where \mathbf{I} is the identity matrix, E is Young's modulus, ν is Poisson's ratio and the strain $\boldsymbol{\varepsilon}$ is a second order tensor. Under infinitesimal deformation, the strain tensor is a function of displacement as

$$\boldsymbol{\varepsilon} = \frac{1}{2} (\nabla^T \mathbf{u} + \nabla \mathbf{u}). \quad (9)$$

2.1 Numerical Discretization

Two discretization schemes will be employed in computational examples which are referred to as *DS1* and *DS2*. *DS1* considers a single fracture in an infinite domain while *DS2* deals with rather general fracture and domain geometry. The simulation test performed only considers the static fracture. The propagation scenario will be investigated in the next section. Both schemes are briefly introduced.

2.1.1 DS1

A single fracture is modeled in an infinite domain as shown in fig. 1a. Due to symmetry, only half of the domain is modeled. According to [16], the aperture field ω is obtained by solving eqs. (5) and (7) to (9), and can be written as an explicit function of p by the Green's function \mathcal{G} ,

$$\begin{aligned}\omega(x) &= -\frac{2(1-\nu^2)}{\pi E} \int_0^a \mathcal{G}(s; x) p(s) ds \\ &= -\frac{2(1-\nu^2)}{\pi E} \int_0^a \ln \left| \frac{(a^2 - x^2)^{\frac{1}{2}} - (a^2 - s^2)^{\frac{1}{2}}}{(a^2 - x^2)^{\frac{1}{2}} + (a^2 - s^2)^{\frac{1}{2}}} \right| p(s) ds\end{aligned}\quad (10)$$

where a is the fracture half length. Consequently, an integro-differential equation system, eqs. (2) and (10), is formulated. Next, a discrete approximation of this formulation is described.

The domain \mathcal{C} is approximated with n_c equally-spaced grid cells using length equal to $\Delta x = \frac{a}{n_c}$. $\boldsymbol{\omega} = \{\omega_i, i = 1, \dots, n_c\}$ and $\boldsymbol{p} = \{p_i, i = 1, \dots, n_c\}$, both of which are co-located at the center of n_c cells. A Gaussian quadrature integration rule is used to evaluate ω_i ,

$$\begin{aligned}\omega_i(x_i = \frac{2i-1}{2}\Delta x) &= -\frac{2(1-\nu^2)}{\pi E} \sum_{j=1}^{n_c} \int_{(j-1)\Delta x}^{j\Delta x} \mathcal{G}(s; x_i) p_j ds \\ &= -\frac{2(1-\nu^2)}{\pi E} \sum_{j=1}^{n_c} \sum_{k=1}^{n_g} \mathcal{G}(s_k^*; x_i) \mathcal{W}_k p_j\end{aligned}\quad (11)$$

where n_g is the number of quadrature points; s_k^* is the quadrature point; \mathcal{W}_k is the weight at the point s_k^* . eq. (11) can be simplified using a matrix-vector notation,

$$\boldsymbol{\omega} = \boldsymbol{A} \boldsymbol{p} \quad (12)$$

where each item in full matrix \boldsymbol{A} stores the numerical integration result of each cell. Since for all s and $x \subseteq (0, a)$, $\mathcal{G}(s; x) < 0$, then $A_{ij} > 0$.

Pertaining to fluid flow, a first-order backward Euler temporal discretization, and a second-order central-difference spatial discretization are applied. The discretized form reads,

$$(\omega_i^{n+1} - \omega_i^n) - T \sum_{\pm} \left(\omega_{i\pm\frac{1}{2}}^{n+1} \right)^3 (p_{i\pm 1}^{n+1} - p_i^{n+1}) = 0 \quad (13)$$

where superscripts n or $n+1$ indicate time level, and $\Delta t = t^{n+1} - t^n$; $T = \frac{\Delta t}{12\mu\Delta x^2}$ is the static transmissibility while ω at the interface is evaluated by the arithmetic average of its neighboring cells', i.e. $\omega_{i\pm\frac{1}{2}} = \frac{\omega_i + \omega_{i\pm 1}}{2}$. Combining eqs. (12) and (13), a matrix-vector form of the nonlinear system is formulated

$$(\boldsymbol{A} + \boldsymbol{F}(\boldsymbol{p}^{n+1})) \boldsymbol{p}^{n+1} = \boldsymbol{q} + \boldsymbol{\omega}^n \quad (14)$$

where $\boldsymbol{q} = (\frac{\Delta t}{\Delta x} Q, 0, \dots, 0)^T$ is a n_c by 1 vector, \boldsymbol{F} represents the flux term and is a tri-diagonal sparse matrix under a 2D setting. The detailed expression of \boldsymbol{F} is given in A.

2.1.2 DS2

In general scenarios with multiple fractures, as well as complex-fracture geometries, the original problem is approximated using a mixed discretization; coupled extended FEM and embedded FVM for mechanics deformation and fluid flow, respectively. The numerical details of the method is referred to the appendix C.

3 Proposed Quasi-Newton Solver

Newton's method is typically applied to solve nonlinear algebraic systems that arise from discretization. It is observed that these methods may converge to nonphysical solutions. In the following subsections, this is analyzed theoretically and empirically in the contexts of models DS1 and DS2 introduced above. Furthermore, a Quasi-Newton approach is proposed, and demonstrated to provide robust global convergence to the physical solution.

3.1 Analysis and development using model DS1

The nonlinear system eq. (14) is to be solved, where the residual vector \mathbf{R} and Jacobian matrix \mathbf{J} in the context of DS1 become,

$$R_i^{n+1,v+1} = (\omega_i^{n+1,v} - \omega_i^n) - T \sum_{\pm} \left(\omega_{i \pm \frac{1}{2}}^{n+1,v} \right)^3 (p_{i \pm 1}^{n+1,v} - p_i^{n+1,v}) - q_i \quad (15a)$$

$$J_{ij}^{n+1,v+1} = \frac{\partial \omega_i^{n+1,v}}{\partial p_j^{n+1,v}} - T \sum_{\pm} \left(\omega_{i \pm \frac{1}{2}}^{n+1,v} \right)^3 \frac{\partial (p_{i \pm 1}^{n+1,v} - p_i^{n+1,v})}{\partial p_j^{n+1,v}} - T \sum_{\pm} \frac{\partial \left(\omega_{i \pm \frac{1}{2}}^{n+1,v} \right)^3}{\partial p_j^{n+1,v}} (p_{i \pm 1}^{n+1,v} - p_i^{n+1,v}) \quad (15b)$$

$$\mathbf{J}^{n+1,v+1} \delta \mathbf{p}^{n+1,v+1} = -\mathbf{R}^{n+1,v+1} \quad (15c)$$

where superscripts v or $v + 1$ represent the iteration level. The first term on the right-hand side (RHS) of eq. (15b), $\frac{\partial \omega_i^{n+1,v}}{\partial p_j^{n+1,v}}$, is equal to A_{ij} ; the second term on the RHS of eq. (15b) forms a diagonally dominant sparse matrix whose diagonal terms are positive and off-diagonal terms are negative. The last term on the RHS of eq. (15b) produces a full matrix with elements consisting of derivatives of ω^3 with respect to p . The subsequent numerical study demonstrates that the presence of this term can lead to convergence of Newton's method to a nonphysical solution. In the proposed Quasi-Newton approach, the third term is neglected in the Jacobian calculation. Note that in [11, 17], a similar strategy is adopted but for the purpose of guaranteeing a monotone linear matrix. The QN method now reads,

$$\tilde{J}_{ij}^{n+1,v+1} = \frac{\partial \omega_i^{n+1,v}}{\partial p_j^{n+1,v}} - T \sum_{\pm} \left(\omega_{i \pm \frac{1}{2}}^{n+1,v} \right)^3 \frac{\partial (p_{i \pm 1}^{n+1,v} - p_i^{n+1,v})}{\partial p_j^{n+1,v}} \quad (16a)$$

$$\tilde{\mathbf{J}}^{n+1,v+1} \mathbf{p}^{n+1,v+1} = (\mathbf{A} + \mathbf{F}(\mathbf{p}^{n+1,v})) \mathbf{p}^{n+1,v+1} = \mathbf{q} + \boldsymbol{\omega}^n \quad (16b)$$

From eq. (16b), a mapping $K : X \rightarrow X$, $X \subset \mathbb{R}^{n_c}$ is defined as

$$K = (\mathbf{A} + \mathbf{F}(\mathbf{p}))^{-1}(\mathbf{q} + \boldsymbol{\omega}^n) \quad (17)$$

Consequently, our Quasi-Newton eq. (16b) searches for fixed points over set X . The following proposition proposes a property on set X ,

Proposition 1. $\forall \mathbf{p} \in X$, mapping $K : X \rightarrow X$, and $X \subset \mathbb{R}^{n_c}$ is a vector space that satisfies $\sum_i (\mathbf{A} \mathbf{p}^*)_i = \sum_i (\mathbf{q} + \boldsymbol{\omega}^n)_i$, where $\mathbf{p}^* = K(\mathbf{p})$.

Proposition 1 states that the total mass balance is satisfied during each iteration. The proof of the Proposition 1 is in Appendix B.

3.1.1 Analysis of fixed-point stability

There may exist multiple fixed-points in X . The stability of such fixed-points for nonlinear mappings K corresponding to both Newton's and Quasi-Newton methods is analyzed. The stability of fixed points is defined by Definition 1.

Definition 1. Fixed-points can be classified as,

- The fixed point \mathbf{p}_0 is stable if there exists an open set $U \subset X$ containing \mathbf{p}_0 such that $\|K(\mathbf{p}) - \mathbf{p}_0\| \leq \|\mathbf{p} - \mathbf{p}_0\|$ for all $\mathbf{p} \in U$
- The fixed point \mathbf{p}_0 is unstable if there exists an open set $U \subset X$ containing \mathbf{p}_0 such that $\|K(\mathbf{p}) - \mathbf{p}_0\| \geq \|\mathbf{p} - \mathbf{p}_0\|$ for all $\mathbf{p} \in U$

A well-studied result in discrete dynamics characterizes the stability of fixed-points for multi-variable nonlinear operators.

Theorem 1. (see [4]) Suppose map $K : X \rightarrow X$ is differentiable at a fixed point \mathbf{p}_0 and then let $\lambda_1, \lambda_2, \dots, \lambda_n$ be the eigenvalues of the Jacobian matrix K' evaluated at \mathbf{p}_0 .

- if all the eigenvalues λ_j have $|\lambda_j| < 1$, then \mathbf{p}_0 is stable or attracting.
- if one eigenvalue λ_{j0} has $|\lambda_{j0}| > 1$, \mathbf{p}_0 is unstable, which can be either saddle or repelling.

- if all the eigenvalues λ_j have $|\lambda_j| > 1$, then \mathbf{p}_0 is repelling.

An empirical analysis of the stability of the fixed-points is conducted. The Buckingham π theorem is applied in a dimensional analysis to yield the following dimensionless groups,

$$\Pi_1 = \frac{\mu}{Et}, \quad \Pi_2 = \frac{qt}{a^2}, \quad \Pi_3 = \frac{p}{E} \quad (18)$$

Based on the Buckingham π theorem, the solution Π_3 only depends on the magnitude of Π_1 and Π_2 . The domain setup is shown in fig. 1a. A single fracture is in the center of an infinite domain. Initially, the fracture is void of fluid, i.e. $\omega^n = 0$. The simulation runs for one time step $\Delta t = t$. The fracture is represented using four grid cells. The input parameter Π_1 is varied across simulations from $1e-17$ to $1.5e-1$ and Π_2 from $1e-5$ to $2e-2$. As a result, there are 8000 simulation cases in total. The physical and nonphysical solutions are generated for each one of 8000 simulation cases. Subsequently, then spectral radius of K' , $\rho(K')$ is evaluated for each case at the physical and nonphysical solutions. These results are illustrated in fig. 2. All nonphysical solutions are unstable fixed-points of the Quasi-Newton mapping, while all physical solutions are stable. In other words, if the Quasi-Newton method converges, it will not do so to a nonphysical solution since any small perturbation will push the next iterate away from the unstable fixed point. To demonstrate this, we apply the nonphysical solution perturbed by 0.01% as an initial guess for the Quasi-Newton method. All 8000 cases converge to the physical solution, with a maximum of 12 nonlinear iterations. The number of nonlinear iterations required to convergence over the entire test-set appears in fig. 3.

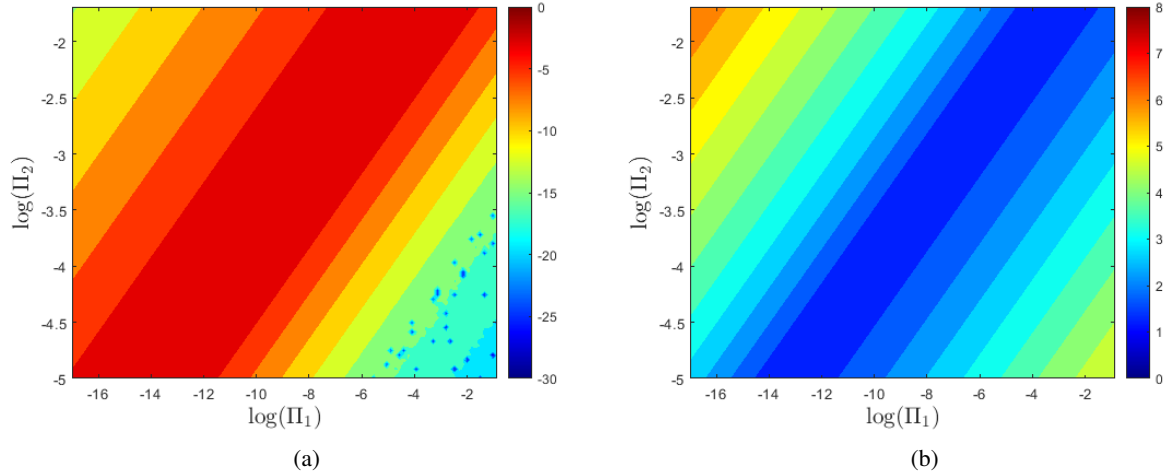


Figure 2: $\log(\rho(K'))$ of Quasi-Newton method v.s $(\log(\Pi_1), \log(\Pi_2))$. (a) physical solution; (b) nonphysical solution.

Similarly, the stability of fixed-points for the Newton operator is also investigated. A mapping K for Newton's method can be defined as,

$$K(\mathbf{p}) = \mathbf{p} - \mathbf{J}^{-1}(\mathbf{p})\mathbf{R}(\mathbf{p}) \quad (19)$$

The computed spectral radius $\rho(K')$ at physical and nonphysical solutions over the investigation space are presented in fig. 4. Clearly, both physical and nonphysical solutions are stable fixed points in X . This explains why Newton's method may converge to the negative aperture solution when applied to any of these problems.

3.1.2 contraction mapping

Definition 2. Let (D, d) define a metric space. Mapping $G : D \rightarrow D$ is a contraction, if there exists a constant c , with $0 < c < 1$, such that

$$d(G(y_1) - G(y_2)) < cd(y_1, y_2) \quad (20)$$

for all $y_1, y_2 \in D$. Note that c in eq. (20) is the Lipschitz constant.

Next, it is demonstrated that a mapping G for ω preserves the contraction mapping property on a certain iteration path. The RHS of eq. (17) is left multiplied by matrix A , to produce G as,

$$G = \mathbf{A}(\mathbf{A} + \mathbf{F}(\omega))^{-1}(\mathbf{q} + \omega^n) \quad (21)$$

Firstly, we define a set D that only contains physical solutions.

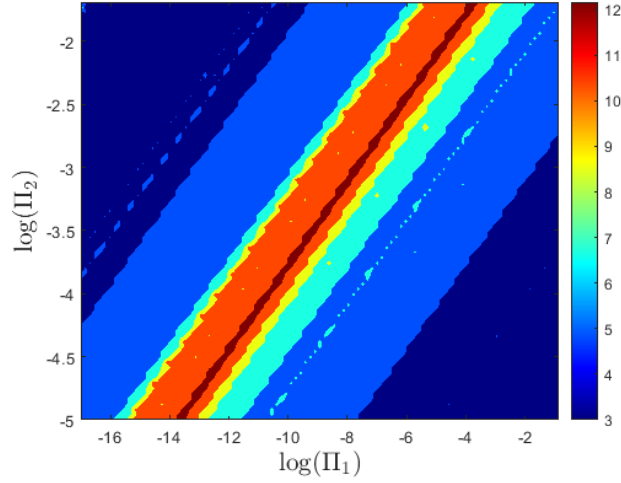


Figure 3: nonlinear iterations of each case using the slightly perturbed nonphysical solution as the initial guess

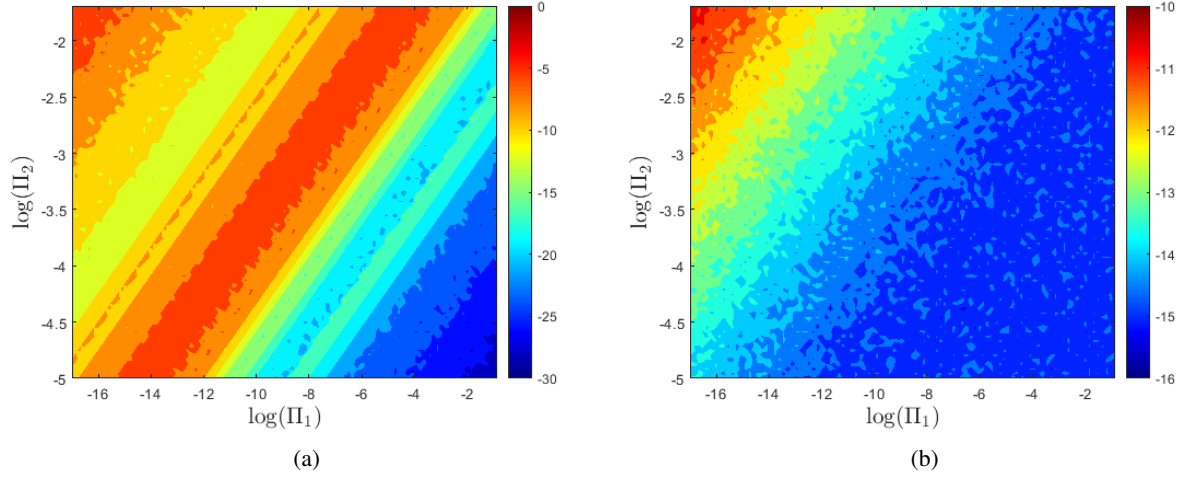


Figure 4: $\log(\rho(K'))$ of Newton's method v.s $(\log(\Pi_1), \log(\Pi_2))$. (a) physical solution; (b) nonphysical solution.

Definition 3. Set D is defined such that dimensionless aperture $\frac{\omega}{\sqrt{Q_t}} \geq \varepsilon_0$. Here ε_0 is a fixed tolerance whose absolute value, $|\varepsilon_0|$, is close to 0.

In order to show there exists a $0 < c < 1$ such that mapping $G : D \rightarrow D$ is a contraction, we design an iteration path for mapping G

$$G = \mathbf{A}(\mathbf{A} + \mathbf{F}(\omega^{n+1,v}))^{-1}(\mathbf{q} + \omega^n) \quad (22)$$

where v stands for applying G for v iterations, and $\omega^{n+1,v}$ is

$$\omega^{n+1,v} = \begin{cases} \omega^n & v = 1 \\ \omega^{n+1,v-1} & v \geq 1 \end{cases} \quad (23)$$

where in the first iteration, the previous time-step solution is applied as the initial guess.

There are two things that need to be demonstrated for a contraction mapping: (1) if $\frac{\omega}{\sqrt{Q_t}} \in D$, $\frac{K(\omega)}{\sqrt{Q_t}} \in D$; (2) there exists $0 < c < 1$ on the designed iteration path, eq. (22) and eq. (23). To present the value of c during the numerical simulation, the following calculation is adopted

$$c = \frac{d(G^v(\omega^v), G^v(\omega^{v-1}))}{d(\omega^v, \omega^{v-1})} = \frac{d(\omega^{v+1}, \omega^v)}{d(\omega^v, \omega^{v-1})} \quad (24)$$

where operator d is chosen as L_2 norm in this manuscript.

The same simulation cases used the analysis of fixed-point stability are used except with $n_c = 15$. The results appear in fig. 5. In fig. 5a, the Lipschitz constant c is below 1 for all simulation cases. The minimum dimensionless aperture $\frac{\omega}{\sqrt{qt}}$ is recorded during the nonlinear iteration. The dark blue area in fig. 5b indicates that all iterations produce an $\omega > 0$. In the yellow and orange regions, ε_0 is on the order of $-1e-5$, which is approximately three orders of magnitude less than the positive values of $\frac{\omega}{\sqrt{qt}}$. In summary, on the designed iteration path, $G(\omega)$ produces aperture $\omega \in D$. fig. 5c shows that the maximum number of iterations needed is below 20.

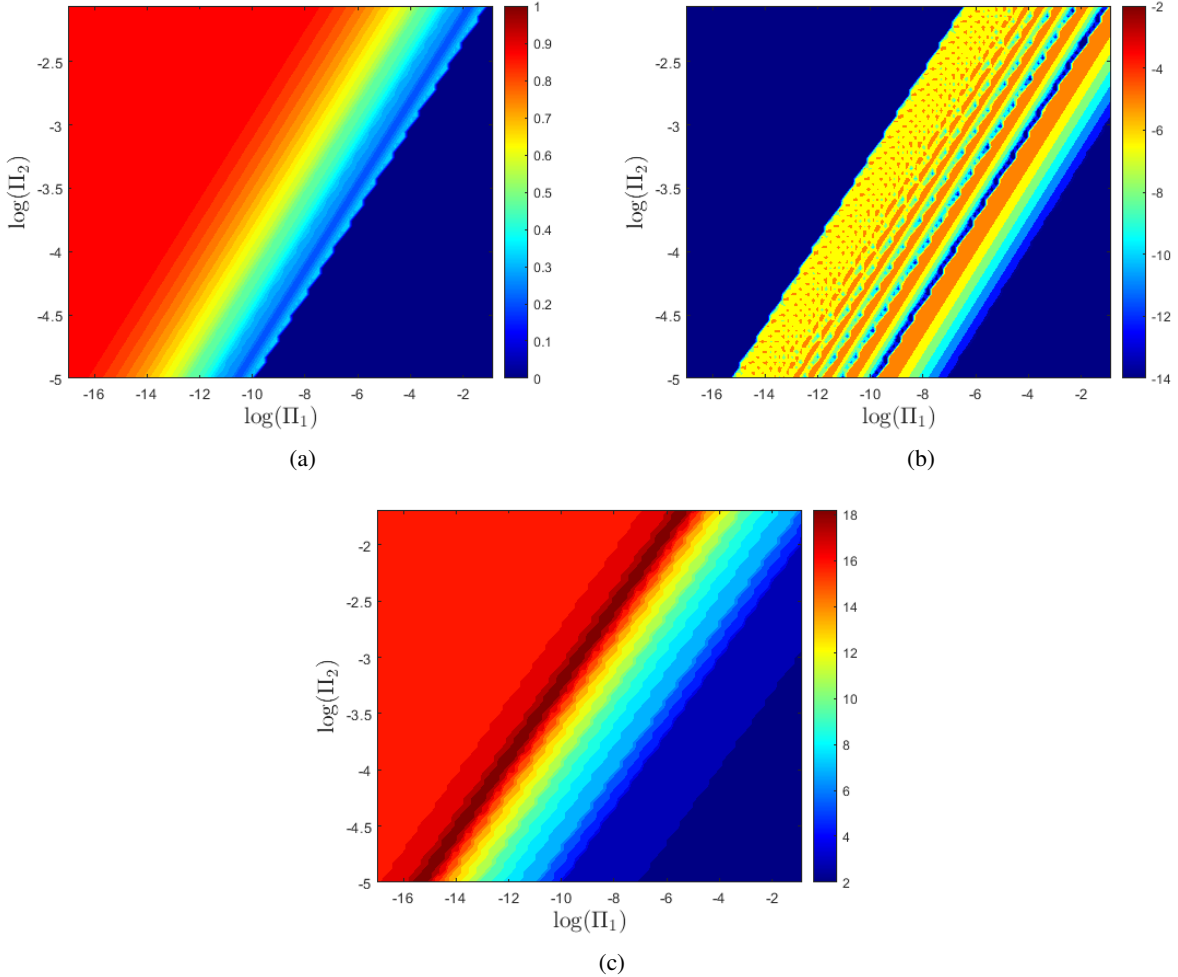


Figure 5: Quasi-Newton Contraction Verification: (a) the maximum c during nonlinear iterations; (b) the minimum dimensionless $\frac{\omega}{\sqrt{qt}}$ during nonlinear iterations and $\log(-\frac{\omega}{\sqrt{qt}})$ is presented; (c) nonlinear iterations for each case.

Remark 1. *Contraction mapping is verified empirically under uniform grid size. In order to maintain the contraction in non-uniform grid systems, a constraint on the time-step size may be enforced.*

Physical interpretations A simulation case using one of the dimensional groups (Π_1, Π_2) in the contraction-mapping test is used to motivate the evolution of ω and p during the proposed Quasi-Newton iteration. In fig. 6, ω and p profiles are captured at different nonlinear iteration numbers, ν . A moving fluid front in the fracture is captured for each iteration. Aperture profiles are split over two sub-regions: A fluid-filled region where $\omega > 0$ and a fluid-void region where $\omega = 0$. As the solver iterates, ω is gradually opened by the fluid front. Similarly, on the pressure profile, the fluid-filled region is represented by positive pressure, whereas the fluid-void space is indicated by negative pressure.

In terms of the structure of \mathbf{F} , the number of nonzero entries in matrix \mathbf{F} increases as the iteration grows. For example, in the first iteration ($\nu = 1$), only the aperture of the first grid cell is positive and, therefore, the only nonzero entries are first and second rows of \mathbf{F} , which means there exists flux between the first and second cells. In the second iteration, since aperture of the first two cells is positive, a third row will be added into nonzero entries of \mathbf{F} . Consequently, the fluid front is moving exactly one grid cell after each iteration. As a result, the number of iterations needed for convergence approximately depends on the number of fracture cells, as well as the fluid front location at the convergence. This in turn, may be interpreted to scale with the target time-size under continued injection.

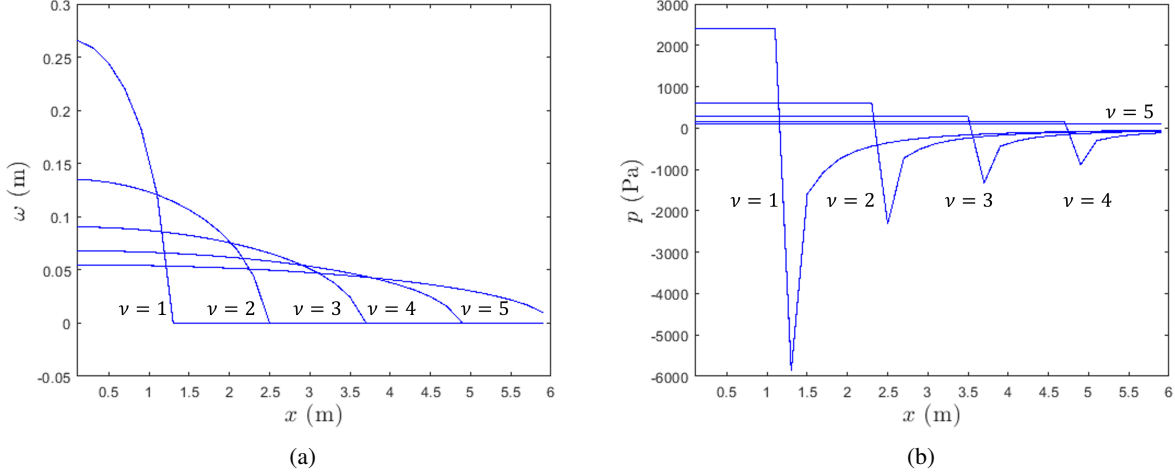


Figure 6: ω and p profiles during Quasi-Newton's iteration. Iteration number, ν , increases from left to right.

3.2 Extension and application to model DS2

The proposed Quasi-Newton formulation is extended to the co-solution of p and u using a general XFEM-FVM discretization. As motivated in the previous section, the contraction mapping property may be verified computationally in terms of ω as an independent-variable. In order to translate to a similar effect for aperture maintained in the coupled XFEM-FVM system, we first derive a nonlinear mapping function similar to eq. (21), and multiple cases are investigated. In the first case, a group of injection tests are conducted in which the Lipschitz constant c is evaluated and analyzed for contraction in aperture. In the second case, the viscosity-dominated KGD problem is studied to show the robustness of the solver. In the final case, multiple fracture propagation is considered and solver performance is reported.

In the XFEM-FVM scheme, XFEM offers a relationship between ω and \mathbf{u} as,

$$\omega = \mathbf{B}\mathbf{u} \quad (25)$$

where \mathbf{B} is a rank-deficient linear matrix. Substituting eq. (25) into eqs. (15a) and (15b) yields the discretized system as well as Jacobian matrix using Quasi-Newton method. A similar form, such as eq. (16b), can be written here for the XFEM-FVM discretized system,

$$\begin{bmatrix} \tilde{\mathbf{J}}_{ff} & \tilde{\mathbf{J}}_{fm} \\ \tilde{\mathbf{J}}_{mf} & \tilde{\mathbf{J}}_{mm} \end{bmatrix}^v \begin{bmatrix} p \\ u \end{bmatrix}^{v+1} = \begin{bmatrix} \mathbf{F}_f \\ \mathbf{F}_m \end{bmatrix} \quad (26)$$

where f, m indicates flow and mechanics, respectively. During iterations, $\tilde{\mathbf{J}}_{ff}$ is a function of ω^v whose values are taken from the previous iteration using eq. (25). In the Quasi-Newton approach, $\tilde{\mathbf{J}}_{fm}$ is the same as \mathbf{B} defined in eq. (25). The rest of the terms in eq. (26) are constant and do not change across iterations. $\mathbf{F}_f = \mathbf{q} + \omega^n$ contains the source or sink terms while \mathbf{F}_m contains the Neumann boundary information.

In order to derive a nonlinear mapping for ω in the current system, the Schur complement is constructed to demonstrate that the solution of ω by eq. (26) is equivalent to ω solution obtained by using the following mapping G ,

$$\omega = G(\omega) = \mathbf{B}\tilde{\mathbf{J}}_{mm}^{-1} \left[\mathbf{F}_m - \tilde{\mathbf{J}}_{mf} \mathbf{S}^{-1} (\mathbf{F}_f - \tilde{\mathbf{J}}_{fm} \tilde{\mathbf{J}}_{mm}^{-1} \mathbf{F}_m) \right] \quad (27)$$

where all of terms in eq. (27) are constant except that the Schur complement \mathbf{S} is a function of ω , which is defined as

$$\mathbf{S} = \tilde{\mathbf{J}}_{ff} - \tilde{\mathbf{J}}_{fm} \tilde{\mathbf{J}}_{mm}^{-1} \tilde{\mathbf{J}}_{mf} \quad (28)$$

Starting from eq. (26), the deformation solution,

$$\mathbf{u} = \tilde{\mathbf{J}}_{mm}^{-1}(\mathbf{F}_m - \tilde{\mathbf{J}}_{mf}\mathbf{p}) \quad (29)$$

and the pore-pressure solution is,

$$\mathbf{p} = \mathbf{S}^{-1}(\mathbf{F}_f - \tilde{\mathbf{J}}_{fm}\tilde{\mathbf{J}}_{mm}^{-1}\mathbf{F}_m) \quad (30)$$

Note that substituting eq. (30) into eq. (29) and left multiplication of the RHS by \mathbf{B} results in eq. (27).

3.2.1 Injection test

A schematic of the case is illustrated in fig. 1a. The length of the domain is 100 m by 100 m. The fracture half-length is taken as 40 m. The displacement at the mid point of four edges is fixed and stresses on the boundaries are assumed to be zero. Initially, the fracture is void of fluid, i.e., $\omega^0 = 0$ m. An injection rate of $0.001 \text{ m}^2/\text{s}$ is applied and a time step Δt is set at 85 s. The Young's modulus and Poisson's ratio for the rock are 8.3 GPa and 0.25, respectively. Plane strain conditions are assumed.

Fluid is injected at the mid-point of the fracture for a single-time step Δt . The mesh sizes and fluid viscosity are varied to verify the designed iteration path offers a contraction mapping using XFEM-FVM, where c with respect to ω is calculated, and the result is shown in table 1. First, c does not exceed 1 in any test case. Secondly, as μ is increased or mesh size is decreased, c decreases. These observations agree with the results in fig. 5a.

Next, time is marched forward with a fixed $\Delta t = 85$ sec until the injected fluid fills the entire fracture. Four different mesh sizes in table 1 with $\mu = 20 \text{ Pa} \cdot \text{s}$ are evaluated. The maximum c in each time step solution and snapshots of ω profiles are shown in fig. 7. In fig. 7b, during injection, ω is gradually opened while the fluid front is moving from the injection point to the fracture tip. Before the injected fluid fills the fracture, c remains below 1 under the four-tested meshes presented in fig. 7a. A higher value of c is a result of subsequently opened fracture segments with each nonlinear iteration. Once the fluid front reaches the fracture tip, c drops significantly below 0.1. A significant drop of c indicates an improvement of local convergence speed.

Table 1: Maximum c during nonlinear iterations (first number in the bracket) and the number of nonlinear iterations (second number in the bracket)

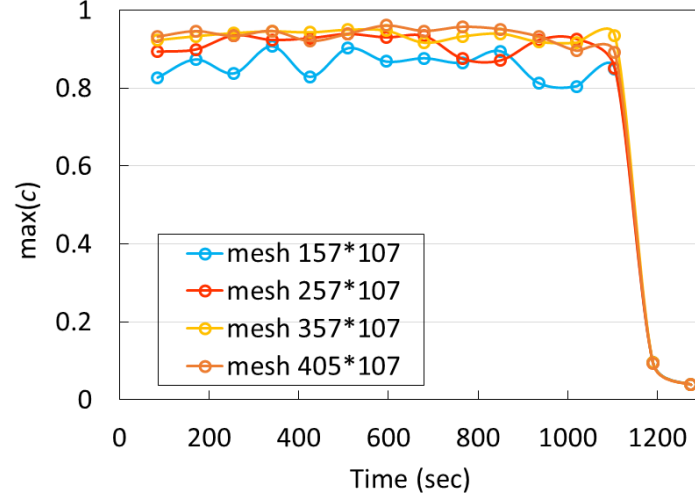
$\mu(\text{Pa} \cdot \text{s})$	20	200	2000	20000
mesh sizes				
157×107	(0.83, 34)	(0.81, 25)	(0.69, 25)	(0.53, 17)
257×107	(0.89, 44)	(0.86, 39)	(0.82, 26)	(0.75, 26)
357×107	(0.92, 51)	(0.89, 40)	(0.87, 42)	(0.76, 35)
405×107	(0.95, 65)	(0.91, 59)	(0.88, 37)	(0.83, 41)

In computational mechanics, the negative aperture is addressed by applying supporting forces on fracture surfaces, also known as contact force. The penalty method or Lagrangian multipliers are widely-used numerical techniques. We briefly describe how the contact force is added into the coupled system in appendix C. However, a reckless application of contact constraints to hydro-mechanics system may not overcome the non-physical solutions. We test various viscosity scenarios under the mesh size 357×107 . Two numerical schemes are considered here: Newton with the penalty method and Quasi-Newton with the penalty method. The results show in fig. 8. First of all, Newton's solver with the penalty method fails for all of test cases here. Newton's method yields giant updates which destroy the nonlinear solver system. Since both physical and nonphysical solutions are stable for Newton's method, direct application of the penalty method will not guide Newton's path to the correct one and give rise to the failure of the nonlinear solver. On the other hand, all Quasi-Newton with the penalty method converges to the physical solution at a slight higher cost than the pure Quasi-Newton method. The Quasi-Newton could possibly produce very small negative aperture which will introduce the penalty method into calculation. Nevertheless, it converges to the correct solution at the end.

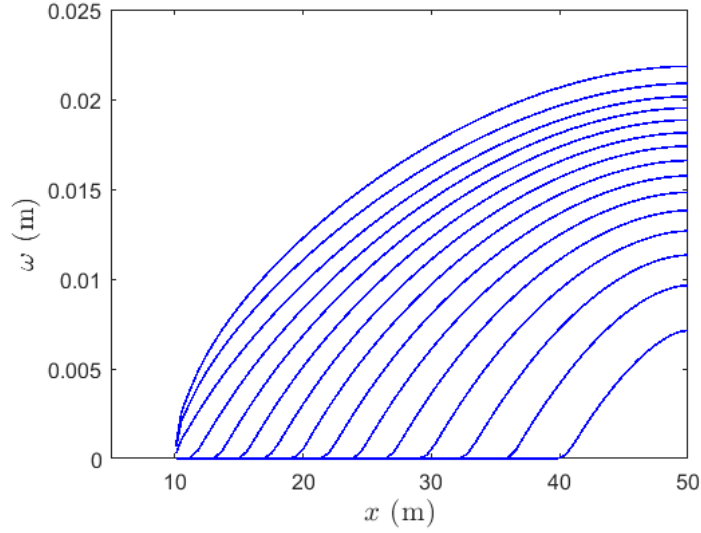
3.2.2 KGD fracture propagation

The proposed method is applied to the simulation of linear-elastic fluid-driven fracture propagation. KGD fracture is considered under two propagation regimes; viscosity-dominated and toughness-dominated. These are controlled by the dimensionless parameter \mathcal{K}_m ([19])

$$\mathcal{K}_m = \frac{8K_c}{(2E'^3\mu'q)^{1/4}}, \quad (31)$$



(a)



(b)

Figure 7: (a) $\max(c)$ of the case $\mu = 20 \text{ Pa} \cdot \text{s}$ recorded at each time step solve; (b) snapshots of ω profiles over half fracture length at different times. Time increases from right to left.

where K_c is the critical stress intensity factor (SIF); $\mu' = 12\mu$, $E' = E/(1 - \nu^2)$ is the equivalent Young's modulus in the plain strain condition; and q is the flow rate into two wings of the fracture. If $\mathcal{K}_m < 1$, the flow lies in the viscosity-dominated regime where rock is very brittle ($K_c \rightarrow 0$) and energy dissipation is dominant in viscous flow. On the other hand, if $\mathcal{K}_m > 4$, the process becomes toughness-dominated regime where energy is mostly used to break the rock and factors from either small aperture or highly-viscous fluid could be neglected.

The rock-failure criterion is based on Irwin's law of linear elastic fracture mechanics and SIF, K_{eq} , is used as an indicator. K_{eq} is never allowed to be larger than the critical K_c during fracture propagation. When $K_{eq} < K_c$, fracture is static. Otherwise, fracture is extended by a certain length Δa defined by the user. In terms of fracture-mesh updates, multiple fracture segments within the same background mesh grid are prohibited. In this way, multiple small fracture segments will be eliminated and large grid-size contrast in the numerical calculation can be avoided. For example, in fig. 9, the fracture segment 3 that partially cuts the grid (fig. 9a) will extend to reach the boundary of the grid (fig. 9b), when fracture propagation is triggered. More details of the fracture propagation algorithm could be referred to appendix D.

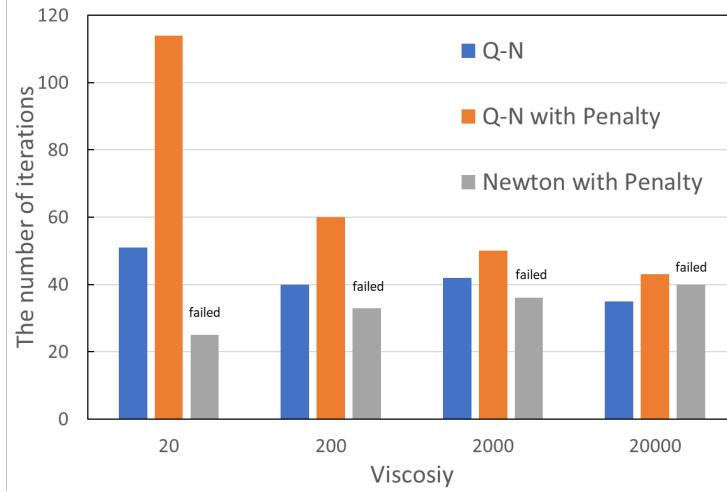


Figure 8: Comparison of three different nonlinear solvers. "failed" above the "Newton with Penalty" bar means the solver fails after a certain number of iterations.

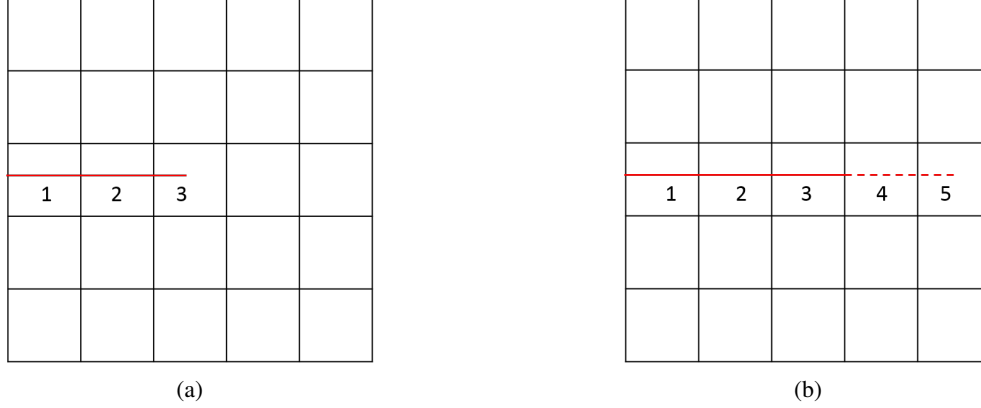


Figure 9: fracture grids and the numbering; (a) before propagation (b) after propagation.

The results suggest that Newton's method is more likely to converge to the nonphysical solution when fracture propagation lies in the viscosity-dominated regime. To further investigate this, consider application of the Quasi-Newton method using the KGD analytical solution in the viscosity-dominated regime.

A square domain of dimensions $100 \times 100 \text{ m}^2$ is modeled with a Cartesian mesh of size 317×117 . The initial fracture position is at the center of the domain with a half length of 2 m. The rock and fluid parameters are listed in table 2 and the maximum time-step size is 0.5 sec. The total simulation time is 90 sec. Two advancement lengths, $\Delta a = 2, 4 \text{ m}$, are applied. The convergence criterion is controlled as,

$$\sqrt{\frac{\sum_{i=1}^N (\omega^{v+1} - \omega^v)^2}{N}} < 1e-8 \quad (32)$$

where N is the number of fracture grids.

Table 2: Input parameters for KGD model verification					
$E(\text{GPa})$	ν	$K_c(\text{MPa}\sqrt{\text{m}})$	$\mu(\text{Pa} \cdot \text{s})$	$q(\text{m}^2/\text{s})$	\mathcal{K}_m
8.3	0.25	0.5	2e-3	0.001	0.78

The viscosity-dominated analytical solution is generated using the form given in [1]. A comparison of numerical and analytical results are illustrated in fig. 10 for both time-step sizes considered. The pressure profile of viscosity-

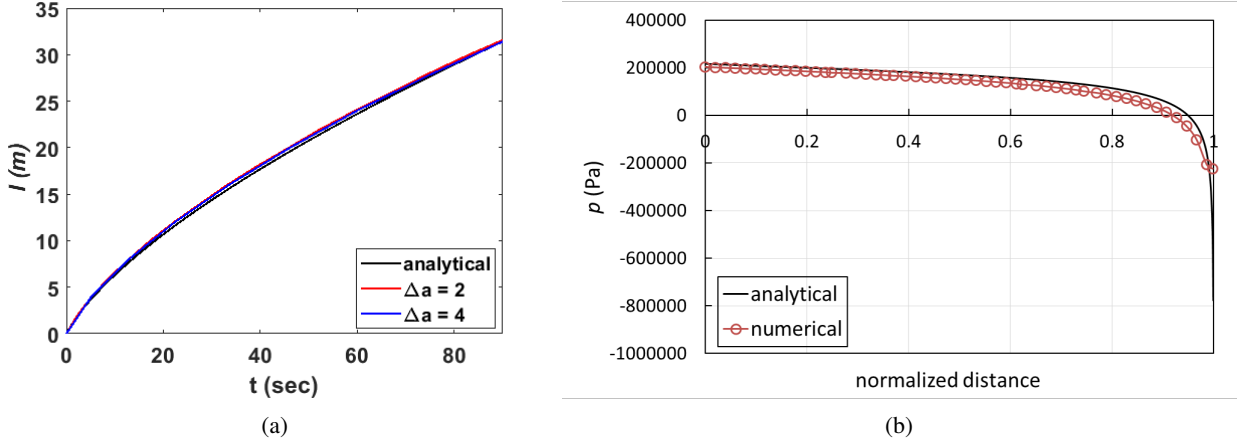


Figure 10: (a) fracture half length evolution with time (b) p profile when half fracture length is equal to 16 m.

dominated fracture propagation exhibits negative values near the tip and asymptotically decays. The singular behavior of pressure at the tip adds additional difficulty to Newton's method in obtaining this physical solution.

During the simulation, the Quasi-Newton approach always converges to the physical solution and the performance is reported in fig. 10. The constant c computed in each iteration over the entire simulation for both step-length sizes are plotted in fig. 11a and fig. 11b. c is below 1, confirming the contraction mapping property on the designed iteration path throughout the course of entire simulation. The number of iterations for each time step is illustrated in fig. 11c and fig. 11b.

3.2.3 multiple fracture propagation

Consider a pre-existing fracture network as illustrated in fig. 12a. In this test case, point source fluid injection into the network and fracture propagation are simulated under various conditions. The input parameters are listed in table 3. The upper and lower boundaries are under the maximum horizontal stress σ_H while the left and right boundaries are under the minimum one σ_h . The point sources are located on the two horizontal fractures at (50, 48) and (50, 52), respectively. The injection rates that equal $0.001 \text{ m}^2/\text{s}$ are the same for two point sources. At $t = 0$, fractures are void of fluid. The simulation time lasts 122 secs.

Table 3: Input parameters for the case of multiple fracture propagation

	value	unit
E	8.3	GPa
ν	0.25	
μ	2e-3	Pa · s
K_c	2e6	Pa $\sqrt{\text{m}}$
Δa	5	m
σ_H	0.4	MPa
σ_h	0.2	MPa

The plots in figs. 12b to 12d capture three snapshots during fracture propagation. At the earliest time, injected fluid first opens two horizontal fractures while the other three vertical fractures are closed due to stresses on the boundaries. In figs. 12b and 12c, as three vertical fractures have the least resistance from far field stresses than the two horizontal ones, vertical fractures are gradually opened by fluid and start to propagate in the vertical direction. In the meantime, only one horizontal fracture starts to propagate. In the latest time shown in fig. 12d, only propagation of the vertical fractures is observed in the vertical direction perpendicular to the minimum principal stress. The number of nonlinear iterations is shown in fig. 13. There are a few times when the iteration number is above 30 since nonuniform-spaced fracture grids are inevitably introduced during fracture propagation. On the other hand, Newton's method is also applied to this case and fails in the first time when a fracture starts to propagate.

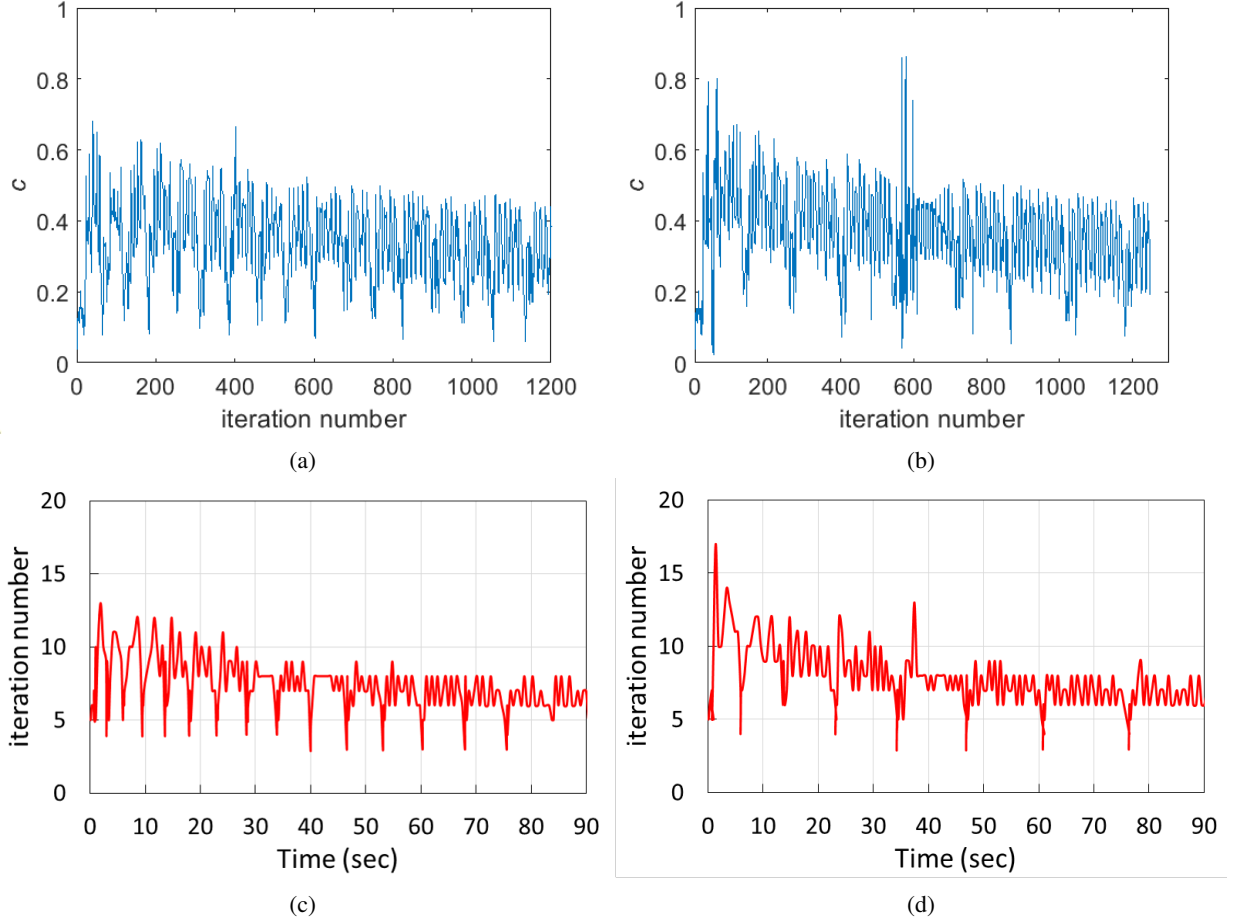


Figure 11: (a) and (b) c over the simulation history (c) and (d) the number of newton iterations in each time step solve. First column corresponds to results with $\Delta a = 2$; Second column corresponds to results with $\Delta a = 4$.

We also rotate σ_H and σ_h on the boundaries and run the same simulation case. In this regard, only two horizontal fractures are advancing in the x direction while three vertical fractures remain static in fig. 14.

4 Discussion and Conclusion

A Quasi-Newton approach is proposed to avoid convergence to nonphysical solutions and to improve solver robustness for coupled hydro-mechanics and fracture propagation simulation. Supported by thorough empirical observation and some analysis, the following findings are listed:

- multiple solutions may exist for coupled hydro-mechanical models of Poiseuille flow in fracture, and this has been observed in fully discrete and semi-analytical models.
- the derivative of the flux function with respect to aperture in the Jacobian matrix can influence the Newton path towards nonphysical solution.
- empirical stability analysis suggests that the physical solution is the only stable fixed point for the proposed Quasi-Newton method, whereas both physical and nonphysical solutions are stable fixed points for Newton's method.
- the proposed Quasi-Newton method is a contraction for aperture on uniform grids.

In fracture propagation, the simulation meshing is adjusted with simulation time. An inappropriate initialization of unknowns in the newly-formed fracture space can possibly steer the nonlinear Newton solution process for state (displacement and pressure) to a nonphysical fixed-point attractor. This more frequently observed in viscosity-dominated

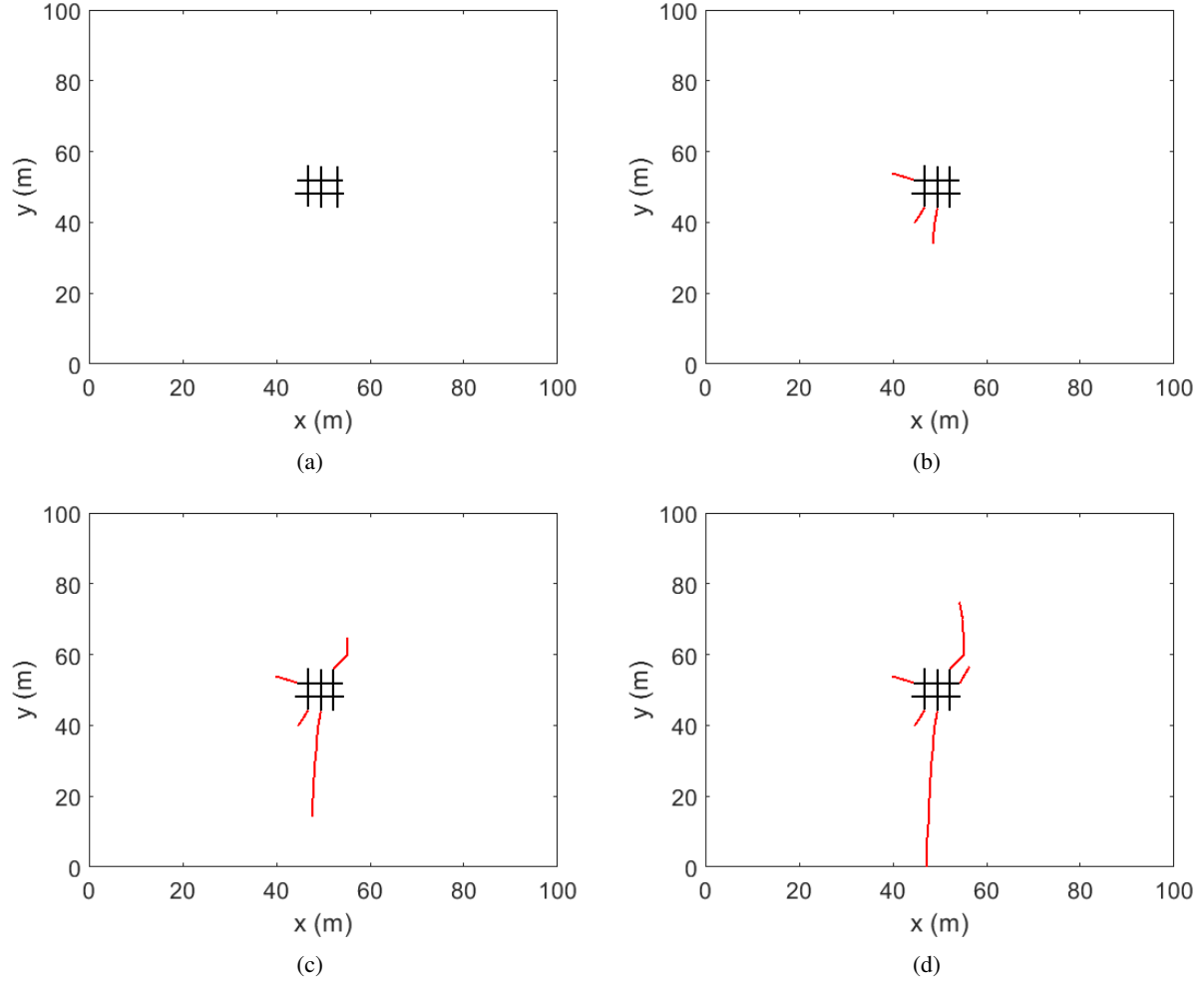


Figure 12: (a) initial fracture configuration; (b) (c) and (d) fracture configurations at three different times in chronological order.

propagation problems. The proposed Quasi-Newton method is demonstrated to overcome these issues in viscosity-dominated KGD fracture propagation, as well as under the simultaneous propagation of multiple fractures. The proposed method has been tested under the setting of a 2D domain, but can be readily extended to 3D domain.

5 Acknowledgements

This material is based upon work supported by the U.S. Department of Energy under Award Number DE-FE-0031777. The authors also acknowledge partial funding from the members of the TU Future Reservoir Simulation Systems & Technology (FuRSST) Industry-University Consortium.

References

- [1] José Ignacio Adachi. Fluid-driven fracture in permeable rock. *PhD thesis*, 2002.
- [2] Zdeněk P Bažant, Marco Salviato, Viet T Chau, Hari Viswanathan, and Aleksander Zubelewicz. Why fracking works. *Journal of Applied Mechanics*, 81(10), 2014.
- [3] Katrin Breede, Khatia Dzebisashvili, Xiaolei Liu, and Gioia Falcone. A systematic review of enhanced (or engineered) geothermal systems: past, present and future. *Geothermal Energy*, 1(1):1–27, 2013.

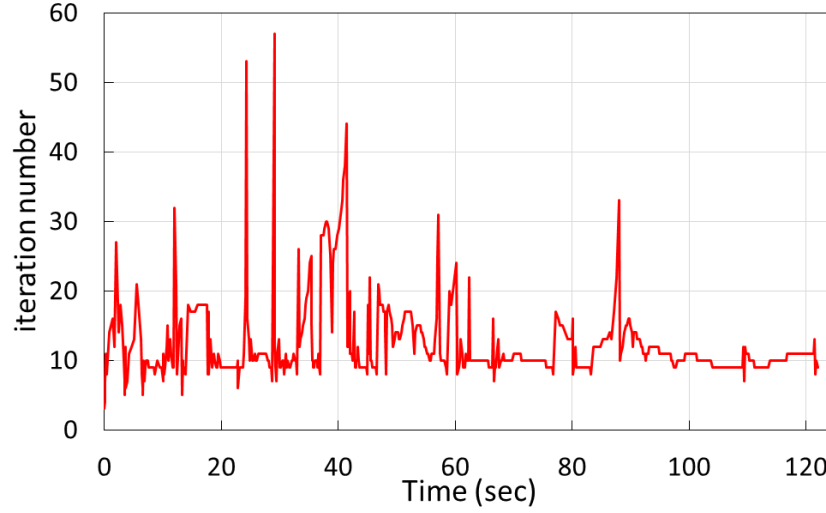
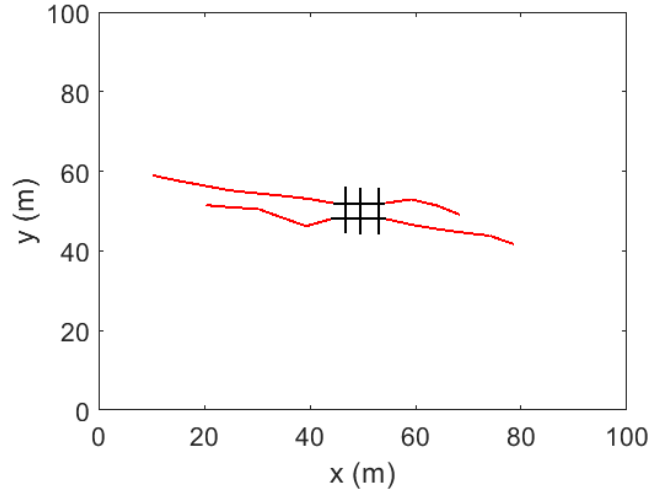


Figure 13: nonlinear iterations for each time step solve

Figure 14: fracture geometry when σ_H is in the horizontal direction and σ_h is in the vertical direction.

- [4] Beatriz Campos, Alicia Cordero, Juan R Torregrosa, and Pura Vindel. Stability of king's family of iterative methods with memory. *Journal of Computational and Applied Mathematics*, 318:504–514, 2017.
- [5] Ryan WJ Edwards, Michael A Celia, Karl W Bandilla, Florian Doster, and Cynthia M Kanno. A model to estimate carbon dioxide injectivity and storage capacity for geological sequestration in shale gas wells. *Environmental science & technology*, 49(15):9222–9229, 2015.
- [6] Vivette Girault, Kundan Kumar, and Mary F Wheeler. Convergence of iterative coupling of geomechanics with flow in a fractured poroelastic medium. *Computational Geosciences*, 20(5):997–1011, 2016.
- [7] Vivette Girault, Mary F Wheeler, Benjamin Ganis, and Mark E Mear. A lubrication fracture model in a poroelastic medium. *Mathematical Models and Methods in Applied Sciences*, 25(04):587–645, 2015.
- [8] Elizaveta Gordeliy and Anthony Peirce. Implicit level set schemes for modeling hydraulic fractures using the xfem. *Computer Methods in Applied Mechanics and Engineering*, 266:125–143, 2013.
- [9] P Gupta and Carlos Armando Duarte. Coupled hydromechanical-fracture simulations of nonplanar three-dimensional hydraulic fracture propagation. *International Journal for Numerical and Analytical Methods in Geomechanics*, 42(1):143–180, 2018.

- [10] Michael J Hunsweck, Yongxing Shen, and Adrián J Lew. A finite element approach to the simulation of hydraulic fractures with lag. *International Journal for Numerical and Analytical Methods in Geomechanics*, 37(9):993–1015, 2013.
- [11] Konstantin Lipnikov, Mikhail Shashkov, Daniil Svyatskiy, and Yu Vassilevski. Monotone finite volume schemes for diffusion equations on unstructured triangular and shape-regular polygonal meshes. *Journal of Computational Physics*, 227(1):492–512, 2007.
- [12] Konstantin Lipnikov, Daniil Svyatskiy, and Yuri Vassilevski. Interpolation-free monotone finite volume method for diffusion equations on polygonal meshes. *Journal of Computational Physics*, 228(3):703–716, 2009.
- [13] Fushen Liu. Modeling hydraulic fracture propagation in permeable media with an embedded strong discontinuity approach. *International Journal for Numerical and Analytical Methods in Geomechanics*, 44(12):1634–1655, 2020.
- [14] Zhe Liu and Albert C Reynolds. History matching an unconventional reservoir with a complex fracture network. In *SPE Reservoir Simulation Conference*. OnePetro, 2019.
- [15] Guotong Ren and Rami M Younis. An integrated numerical model for coupled poro-hydro-mechanics and fracture propagation using embedded meshes. *Computer Methods in Applied Mechanics and Engineering*, 376:113606, 2021.
- [16] DA Spence and P Sharp. Self-similar solutions for elastohydrodynamic cavity flow. *Proceedings of the Royal Society of London. A. Mathematical and Physical Sciences*, 400(1819):289–313, 1985.
- [17] Kirill M Terekhov, Bradley T Mallison, and Hamdi A Tchelepi. Cell-centered nonlinear finite-volume methods for the heterogeneous anisotropic diffusion problem. *Journal of Computational Physics*, 330:245–267, 2017.
- [18] Shiqian Xu, Guotong Ren, Rami M Younis, and Qihong Feng. Revisiting field estimates for carbon dioxide storage in depleted shale gas reservoirs: The role of geomechanics. *International Journal of Greenhouse Gas Control*, 105:103222, 2021.
- [19] Qinglei Zeng, Zhanli Liu, Tao Wang, Yue Gao, and Zhuo Zhuang. Fully coupled simulation of multiple hydraulic fractures to propagate simultaneously from a perforated horizontal wellbore. *Computational Mechanics*, 61(1):137–155, 2018.

A

Matrix \mathbf{F} from eq. (14) is

$$\mathbf{F} = \frac{\Delta t}{12\mu\Delta x^2} \begin{pmatrix} \omega_{1+\frac{1}{2}}^3 & -\omega_{1+\frac{1}{2}}^3 & 0 & 0 & \dots & 0 \\ -\omega_{1+\frac{1}{2}}^3 & \omega_{1+\frac{1}{2}}^3 + \omega_{2+\frac{1}{2}}^3 & -\omega_{2+\frac{1}{2}}^3 & 0 & \dots & 0 \\ \vdots & \vdots & \vdots & \vdots & \ddots & \vdots \\ 0 & 0 & 0 & 0 & -\omega_{n-\frac{1}{2}}^3 & \omega_{n-\frac{1}{2}}^3 \end{pmatrix} \quad (33)$$

where each row and column sum of \mathbf{F} is 0.

B

Proof of Proposition 1

Proof. According to eq. (16b)

$$\mathbf{A}\mathbf{p}^* + \mathbf{F}(\mathbf{p})\mathbf{p}^* = \mathbf{q} + \boldsymbol{\omega}^n \quad (34)$$

Take the column sum of eq. (34), we get

$$\sum_i (\mathbf{A}\mathbf{p}^*)_i + \sum_i (\mathbf{F}(\mathbf{p})\mathbf{p}^*)_i = \sum_i (\mathbf{q} + \boldsymbol{\omega}^n)_i \quad (35)$$

Since $\forall \mathbf{p} \in \mathbb{R}^{n_c}$, $\sum_i (\mathbf{F}(\mathbf{p}))_{ij} = \sum_j (\mathbf{F}(\mathbf{p}))_{ij} = 0$, then $\sum_i (\mathbf{F}(\mathbf{p})\mathbf{p}^*)_i = 0$. Suppose the linear solver can yield the exact solution of \mathbf{p}^* , then Proof 1 is valid. \square

C

The discretization of the proposed the coupled FVM-XFEM will be briefly described in this section. First, flow in the fracture is handled by the finite difference method and its discretized form is the same as eq. (15). On the other side, the displacement approximation of XFEM is

$$\mathbf{u} = \sum_{i \in I} N_i \bar{\mathbf{u}}_i + \sum_{i \in L} N_i (H_c - H_c^i) \bar{\mathbf{a}}_i + \sum_{i \in K} \sum_{l=1}^4 N_i (F_l - F_l^i) \bar{\mathbf{b}}_i^l \quad (36)$$

where I, L, K is the set of standard nodes, Heaviside-enriched nodes and tip-enriched nodes, respectively. N_i is the shape function, H_c is the Heaviside function, and F_l is the tip enrichment function. Expressions for the function above are listed in [15]. $\bar{\mathbf{u}}_i$ is the standard nodal displacement, $\bar{\mathbf{a}}_i$ is Heaviside-enriched nodal displacement, and $\bar{\mathbf{b}}_i^l$ is tip-enriched nodal displacement. Starting from the weak form of eq. (5)

$$\int_{\Omega} \delta \varepsilon : \boldsymbol{\sigma} d\mathbf{x} = \int_{\Gamma_t} \delta \bar{\mathbf{u}} \cdot \mathbf{t} d\mathbf{x} + \int_C \llbracket \delta \bar{\mathbf{u}} \rrbracket \cdot p_F \mathbf{n}_c d\mathbf{x} \quad (37)$$

where $\delta \varepsilon$ and $\delta \bar{\mathbf{u}}$ are the trial functions. Substitution of eq. (36) into the weak form obtains

$$(\delta \bar{\mathbf{u}})^T \sum_{e=1}^N \int_{\Omega^e} (\mathbf{B}_i^r)^T D \mathbf{B}_j^s d\mathbf{x} \bar{\mathbf{u}} = (\delta \bar{\mathbf{u}})^T \sum_{e=1}^{N_c} \left(\int_{C^e} N_i \llbracket F_l \rrbracket p_F \mathbf{n}_c d\mathbf{x} + \int_{C^e} N_i \llbracket H_{\gamma_c} \rrbracket p_F \mathbf{n}_c d\mathbf{x} \right) + (\delta \bar{\mathbf{u}})^T \sum_{e=1}^{N_{\gamma}} \int_{\Gamma_t^e} N_i \mathbf{t} d\mathbf{x} \quad (38)$$

where $r, s = u, a, b^l$, $B^{r,s}$ are the (enriched) shape functions derivatives with respect to coordinates. N is the total number of grid blocks, N_c is the number of fracture grids and N_{γ} is the number of grids along the domain outer boundaries.

The aperture ω can be derived from eq. (36)

$$\omega = 2 \sum_{i \in L} N_i \bar{\mathbf{a}}_i + \sum_{i \in K} \sum_{l=1}^4 N_i (F_l^+ - F_l^-) \bar{\mathbf{b}}_i^l \quad (39)$$

eq. (26) can be obtained using the discretized form of XFEM and FVM. The resultant Newton's linearized system reads

$$\begin{pmatrix} J_{ff} & J_{fm} \\ J_{mf} & J_{mm} \end{pmatrix} \begin{pmatrix} \delta p \\ \delta \mathbf{u} \end{pmatrix} = - \begin{pmatrix} R_f \\ R_m \end{pmatrix}, \quad (40)$$

Where $J_{ff}, J_{fm}, J_{mf}, J_{mm}$ are residuals' derivatives with respect to pressure and displacement. The quasi-newton method can be achieved by modification of J_{fm} . To add contact force into the system, we adopt the penalty method and the weak form now becomes

$$\int_{\Omega} \delta \varepsilon : \boldsymbol{\sigma} d\mathbf{x} = \int_{\Gamma_t} \delta \bar{\mathbf{u}} \cdot \mathbf{t} d\mathbf{x} + \int_C \llbracket \delta \bar{\mathbf{u}} \rrbracket \cdot p_F \mathbf{n}_c d\mathbf{x} + \int_C \llbracket \delta \bar{\mathbf{u}} \rrbracket \cdot (-K_{ct} \omega) \mathbf{n}_c d\mathbf{x} \quad (41)$$

where K_{ct} is the stiffness of the contact. Hence, the discretized form becomes

$$(\delta \bar{\mathbf{u}})^T \sum_{e=1}^N \int_{\Omega^e} (\mathbf{B}_i^r)^T D \mathbf{B}_j^s d\mathbf{x} \bar{\mathbf{u}} = (\delta \bar{\mathbf{u}})^T \sum_{e=1}^{N_c} \left(\int_{C^e} N_i \llbracket F_l \rrbracket p_F \mathbf{n}_c d\mathbf{x} + \int_{C^e} N_i \llbracket H_{\gamma_c} \rrbracket p_F \mathbf{n}_c d\mathbf{x} \right) + (\delta \bar{\mathbf{u}})^T \sum_{e=1}^{N_{\gamma}} \int_{\Gamma_t^e} N_i \mathbf{t} d\mathbf{x} \quad (42)$$

$$+ (\delta \bar{\mathbf{u}})^T \sum_{e=1}^{N_{ct}} \left(\int_{C^e} N_i \llbracket F_l \rrbracket (-K_{ct} \omega) \mathbf{n}_c d\mathbf{x} + \int_{C^e} N_i \llbracket H_{\gamma_c} \rrbracket (-K_{ct} \omega) \mathbf{n}_c d\mathbf{x} \right) \quad (43)$$

where N_{ct} denotes the number of fracture elements whose ω are negative.

D

The fracture propagation algorithm of [15] will be briefly described in this section. The goal is to capture the time spot t_c when the stress intensity factor reaches the critical value,

$$K_{eq} = K_c \quad (44)$$

Two time-step adjustment mechanisms are involved here,

$$\Delta t^{n+1} := \begin{cases} \alpha \Delta t^n & K_{eq} < K_c \\ \frac{K_c - K_{eq}^{old}}{K_{eq} - K_{eq}^{old}} \Delta t^n & K_{eq} > K_c \end{cases} \quad (45)$$

where α is the growth factor. $t^{n+1} = t^n + \Delta t^n$. K_{eq}^{old} and K_{eq} is recorded at t^n and t^{n+1} , respectively. For each time-step solve, the coupled system eq. (40) is solved till eq. (44) is achieved.